

# Optical integral field spectroscopy of the extended line emission around six radio-loud quasars

C.S. Crawford<sup>1,†</sup> & C. Vanderriest<sup>2</sup>

*1. Institute of Astronomy, Madingley Road, Cambridge CB3 0HA*

*2. Observatoire de Paris-Meudon (DAEC), 92195 Meudon Cedex, France*

*† Visiting Astronomer, Canada-France-Hawaii Telescope, which is operated by the National Research Council of Canada, Centre National de Recherche Scientifique, and the University of Hawaii.*

3 October 2018

## ABSTRACT

We present integral field spectroscopy of a small sample of radio-loud quasars at intermediate redshift ( $0.26 < z < 0.60$ ), most of which are associated with large radio sources. All have oxygen line emission extended over tens of kiloparsecs, and these nebulae display a diverse range in both morphology and kinematic behaviour. Two quasars show ‘plumes’ of extended line emission, two show a clumpy structure and a further one shows a smooth distribution. There is no clear pattern with regard to the distribution of the ionized gas in relation to the radio source axis; the extended emission-line regions are found both parallel and perpendicular – and also totally unrelated to – the radio axis. The velocity structure of the ionized gas ranges from essentially static to apparent smooth rotation, and in two cases, show a clear association with the radio source. Given the disparity in properties, the nebulae all show a surprisingly similar ionization state, as measured by the extended lines of [OII] $\lambda$ 3727 and [OIII] $\lambda$ 5007. Assuming the gas is ionized by at least the nearby quasar nucleus, we use the emission line ratios to infer a pressure in the ionized gas; in all cases we find it to be at high pressure, suggesting confinement by an external (probably intracluster) medium.

**Key words:** Galaxies: clusters: general – cooling flows – Quasars: emission lines – Quasars: individual: 3C215, 3C281, 4C37.43, 3C323.1, 3C334, 4C11.72.

## 1 INTRODUCTION

Spatially extended emission-line regions are commonplace around steep-spectrum radio-loud quasars; at low (Stockton & MacKenty 1987, hereafter SM87; Crawford, Fabian & Johnstone 1988; Hutchings & Crampton 1990; Durret et al. 1994; Boisson et al. 1994), intermediate (Crawford & Fabian 1989; Forbes et al. 1990; Hutchings 1992; Bremer et al. 1992; Ridgway & Stockton 1998) and high redshift (Heckman et al. 1991a,b). The gas emits strongly in the coolants of Ly $\alpha$ , [OII] $\lambda$ 3727 and [OIII] $\lambda$ 5007 over radii of tens to a hundred kpc from the quasar nucleus, thus providing a relatively direct way to study of the immediate environment of a quasar beyond its host galaxy. The spatial distribution of the ionized gas appears highly structured into clumps and filaments, but does not appear to be well correlated with any extended continuum structure (SM87). Despite the statistical association of the presence of an EELR with steep-spectrum radio emission, few objects at low redshift show any clear morphological relation of the extended emission-line region

(EELR) to the extended radio source structure (SM87; Hes, Barthel & Fosbury 1996). An alignment of the principal axes is seen more obviously at earlier epochs (Heckman et al. 1991a,b; Crawford & Vanderriest 1997; Ridgway & Stockton 1998).

The distribution of the ionized gas and extended continuum (particularly when elongated into putative tidal tails) is often taken as indicative of the emitting gas – and probably the quasar nuclear activity – originating in a gravitational interaction between the quasar host galaxy and a nearby companion (SM87; Hutchings & Neff 1992; Stockton & Ridgway 1991; Durret et al. 1994; Chatzichristou, Vanderriest & Jaffe 1999). The kinematic structure of the ionized gas, however, where mapped shows no obvious organized pattern, being chaotic and sometimes split into several velocity components (Hickson & Hutchings 1987; Durret et al. 1994).

Off-nuclear spectroscopy of the extended oxygen emission shows the emitting gas to be of surprisingly low ioniza-

tion given its proximity to a luminous quasar nucleus (Crawford & Fabian 1989; Forbes et al. 1990; Bremer et al. 1992; Boisson et al. 1994; Heckman et al. 1991a; Crawford & Vanderriest 1997). The pressure of the gas is deduced to be high, typically  $kT > 4 \times 10^6 \text{ cm}^{-3} \text{ K}$  within 20 kpc of the quasar; if unconfined, this will disperse rapidly on less than a crossing time. To avoid this – given the frequent occurrence of such systems and their apparently chaotic velocity structure – either an exceptionally large reservoir of neutral gas is required, or the EELR must be confined within a high-pressure environment. The inferred pressure is consistent with that in the hot intracluster medium of groups and clusters of galaxies (eg Fabian 1994 and references therein). There is plentiful additional evidence from other wavebands to support the idea that powerful intermediate-(and higher-)redshift radio sources lie in environments richer than the field: from excess galaxy counts (Yee & Green 1984, 1987; Yates et al 1989; Hill & Lilly 1991; Ellingson, Yee & Green 1991; Dickinson 1997), host continuum profiles that resemble cD galaxies (Best et al 1998) and gravitational lensing signatures (Bower & Smail 1997; Deltorn et al 1997), to asymmetric Faraday radio depolarization (Garrington & Conway 1991), sources with very high Faraday rotation measures (Carilli et al. 1994, 1997) and direct X-ray detection of the environment (Crawford & Fabian 1993; Worrall et al. 1994; Crawford & Fabian 1995, 1996a,b; Crawford et al. 1999; Dickinson et al. 1999; Hardcastle & Worrall 1999). A surrounding intracluster medium could possibly provide fuel for the nuclear activity from a cooling flow gravitationally focussed to the quasar (Fabian & Crawford 1990).

Much of the previous work on quasar EELRs has had to rely on either narrow-band imaging of the whole structure, or spectroscopy of only a small region of the gas. In this paper we present optical area spectroscopy of a small sample of low redshift ( $0.2 \leq z \leq 0.6$ ) radio-loud quasars in order to gain a complete picture of the ionized gas by combining direct information on its distribution, ionization state and kinematics over the whole nebula. Connections and comparisons can then be made both directly between these properties and those of the associated radio source.

Only a few low- to intermediate-redshift quasars have been previously targeted using integral field spectroscopy. Durret et al. (1994) presented optical area spectroscopy of three low-redshift quasars, two of which are in common with the sample presented here. The EELR were found to have a clumpy distribution, with discrete blobs embedded in a more diffuse envelope surrounding the quasar. The velocity fields were chaotic, not simply fit by a single rotating disk model. We have presented area spectroscopy data of the exceptional line emission associated with the  $z = 0.734$  radio-loud quasar 3C254 (Crawford & Vanderriest 1997). The ARGUS instrument used (Vanderriest 1995; Chatzichristou et al 1999) allows a larger aperture and a wider wavelength range to be used than the TIGRE system in Durret et al. (1994). The kinematics and distribution of the large EELR around 3C254 strongly indicate an interaction of a radio jet with a dense cloud of ionized gas; however this appears to have little effect on the ionization state of the gas, which remains low in this region.

The layout of this paper is as follows: we detail the observations and data reduction in section 2; section 3 presents a brief introduction to and our results on each of the six

quasars in order of increasing redshift; we summarize and discuss our findings in section 4; finally, conclusions are presented in section 5.

## 2 OBSERVATIONS

### 2.1 Sample selection

We selected our targets from those radio-loud quasars already known to possess spatially extended emission-line regions at the time of the observations, and with a redshift  $z < 0.8$  such that both the dominant emission lines of [OII] $\lambda 3727$  and [OIII] $\lambda 5007$  could be observed. In addition, we chose quasars with a range of radio source properties – from fairly compact to very extended – from those thought to lie in groups and clusters of galaxies. Additional considerations included whether an X-ray flux from the quasar was known at the time, enabling a better knowledge of the photo-ionizing continuum from the nucleus.

### 2.2 Observations and Data reduction

The targets were observed using the integral field spectroscopy device ARGUS on the Canada-France-Hawaii Telescope during the nights of 1993 June 24-27, except for the observation of 3C215 which was observed on the night of 1995 Jan 7. ARGUS is an additional mode to the MOS-SIS spectrograph on the CFHT (Vanderriest 1995) which uses a flexible bundle of optical fibres to transform independent spectra collected at an  $\sim 8.5 \times 12.4$  arcsec hexagonal aperture in the Cassegrain focal plane, into a ‘pseudo’ long-slit for collimation through the MOS. Each fibre has a diameter of 0.4 arcsec, and the spectral range and resolution of the observation are determined only by the CCD and grism used in MOS, the same for all the field of view. The weather conditions were photometric, with seeing conditions typically just sub-arcsecond. The total exposure on each quasar was obtained by co-adding consecutive observations of 1500-2500 s each; a log of observations is given in Table 1. The Loral 3 CCD was used with the O300 grism, leading to a wavelength coverage of 3980–9680Å (the combined CCD and grism efficiency is effectively zero below 3980Å) at a dispersion of 3Å per pixel and a spectral resolution of  $\sim 11$ Å. The ARGUS aperture was oriented with north to the top of the aperture for all the observations in June 1993, and with north toward the top left-hand corner of the aperture for the observation of 3C215 in Jan 1995.

The data were reduced in IRAF using the steps described in detail for the quasar 3C254 in Crawford & Vanderriest (1996). In summary, after correction for bad CCD columns, the individual frames of each quasar were median-combined to remove cosmic ray events and then bias-subtracted (with a bias estimated from the zero response at the blue-wavelength part of the chip). The data were corrected for spatial distortion, flat-fielded using a normalised exposure of a tungsten lamp, and wavelength-calibrated using exposures of a Neon-Helium lamp. They were then flux-calibrated, corrected for both atmospheric extinction, and for Galactic reddening along the line of sight (by the  $A_V$  listed in Table 1, which was estimated from Galactic hydrogen column densities in the direction of each quasar ;Stark

**Table 1.** Log of the observations.

	Name	Redshift	Date	Airmass	Exposure (sec)	$A_V$	Seeing (arcsec)	position angle (degrees)	
	0903+169	3C215	0.412	Jan 95	1.212	7000	0.240	0.8	-45
	1305+069	3C281	0.599	Jun 93	1.346	7500	0.143	0.8	0
	1512+370	4C37.43	0.371	Jun 93	1.316	4500	0.092	0.8	0
	1545+210	3C323.1	0.266	Jun 93	1.102	4000	0.287	1.0	0
	1618+177	3C334	0.555	Jun 93	1.144	5400	0.274	1.0	0
	2251+113	4C11.72	0.323	Jun 93	1.036	6500	0.336	1.1	0

et al. 1992), and converted using the relation of Bohlin, Savage & Drake (1978), assuming  $R$  of 3.2 and the reddening law of Cardelli, Clayton & Mathis (1989)). The data were then separated into spectra from individual fibres. Sky (and scattered-light) subtraction used the average spectrum from fibres that were neither too near the edge of the aperture, nor too close to the source itself; typically a total of 5 or 6 sky fibres per row. A separate sky spectrum was constructed to subtract from each row of the hexagon, using the mean spectrum of all chosen sky fibres in that and the two adjacent rows.

Like the data presented in Crawford & Vanderriest (1996; 1997), the flux calibration is imperfect in that some flux has been lost from the calibration data at wavelengths greater than 7000Å. In practice this has little consequence for the observations presented here, as we are modelling the dynamics, distribution and ionization state of the extended emission-line region (EELR) using the [OII] $\lambda$ 3727, H $\beta$  and [OIII] $\lambda$ 5007 emission lines. Only two of our sample quasars (3C281 and 3C334) are at high enough redshift for some of the lines to be observed at wavelengths appreciably beyond 7000Å. For these two quasars the flux calibration error has been simply corrected by comparing the well-defined power-law slope of the quasar nuclear continuum to high-quality optical/UV spectra in the literature (c.f. CV96). Even if this correction is not sufficient, only widely-spaced line intensity ratios (eg. [OII]/[OIII]) may be affected in these two quasars – the morphology of the EELR, its dynamics, and its ionization state as deduced from the [OIII]/H $\beta$  intensity ratio are not affected. (The error in flux calibration is the same all over the aperture, CV96.)

Arc-lamp exposures were used to characterize fibre-to-fibre variations in the spectral output across the aperture, at the wavelengths of redshifted [OIII] (and [OII], if observed) in each quasar. Variations across the aperture include a decrease in the instrumental resolution toward the edge of the aperture in the blue, and also slight systematic shifts in line wavelength between fibres (CV96). The results of the arc-line fitting are used to remove these systematics from the emission-line results presented in this paper

### 2.3 Emission-line fitting

The spectral fitting of the emission lines was done using QDP (Tennant 1991). Small complexes of neighbouring lines were fit together (eg narrow and broad H $\beta$  with [OIII] $\lambda$ 4959,5007) over a wavelength range of a few hundred Ångströms in each individual fibre spectrum. Narrow lines within such a complex were constrained to have the

same redshift and velocity width as each other, and were fit by a Gaussian (a satisfactory fit even to the [OII] doublet at this resolution). Where an emission line was unresolved (generally only toward the edges of the ARGUS aperture), the FWHM used in the fitting was fixed at an average of the immediately neighbouring fibres' line fits.

## 3 RESULTS

We present an introduction to and results for individual quasars in order of increasing redshift.

### 3.1 3C323.1, $z=0.266$

3C323.1 is one of the nearest radio-loud quasars, and is located on the outskirts of the compact cluster of galaxies Z1545.1+2104 (Oemler, Gunn & Oke 1972; Hintzen & Scott 1978; Yee & Green 1984). It is associated with a steep-spectrum triple radio source which is straight and symmetric over a  $\sim 360$  kpc diameter (Bogers et al. 1994). The quasar lies in a luminous elliptical host galaxy (Neugebauer, Matthews & Armus 1995; Bahcall et al. 1997), with several continuum companions. The dominant companion is a compact galaxy located 2.7 arcsec approximately West at a similar redshift to the quasar (Neugebauer et al. 1995; Canalizo & Stockton 1997); there are two other objects in the field, one at 19 arcsec East and one further North (eg McLeod & Rieke 1994; Hes et al. 1996). Hutchings, Johnson & Pyke (1988) find continuum condensations 1.3 arcsec NW and 3 arcsec S, after subtraction of the quasar light. 3C323.1 has long been known to show an asymmetric emission-line region, extended approximately from south-east to west across the quasar core (SM87; Hes et al. 1996).

The spectral shape of the broad H $\beta$  emission line is slightly skew (eg Brotherton 1996) and thus not perfectly fit by a symmetric gaussian centred about the narrow line component; otherwise fitting models to [OIII]+H $\beta$  in QDP is straightforward. Whilst the ARGUS aperture encompasses the companion galaxy to the west of the quasar core, the continuum detection level of our observation is not sufficiently sensitive to detect it (the efficiency of the ARGUS system is only around half that of a long-slit spectrum). We detect the continuum light from the host galaxy of the quasar as marginally more extended than the (combined MOS+ARGUS) instrumental point-spread function (PSF), similar to the (slightly asymmetric) distribution of the quasar in seen in broad H $\beta$ . We present reconstructed images of 3C323.1 in the light of broad H $\beta$  and [OIII] in

Please see separate figure

**Figure 1.** Reconstructed ARGUS images of 3C323.1 in [OIII] $\lambda$ 5007 intensity (top left; plotted on a scale of 0 (white) to a maximum (black) of  $4.45 \times 10^{-15} \text{ erg cm}^{-2} \text{ s}^{-1}$ , the lowest detection being  $0.03 \times 10^{-15} \text{ erg cm}^{-2} \text{ s}^{-1}$ ); in radial velocity of the [OIII] $\lambda$ 5007 line relative to the nucleus (middle right; on a scale from  $-360$  to  $250 \text{ km s}^{-1}$  as shown in the colour bar); and in broad H $\beta$  intensity showing the approximate PSF of the observation (lower left; plotted on a scale of  $0 - 11.28 \times 10^{-15} \text{ erg cm}^{-2} \text{ s}^{-1}$  with a minimum detection of  $0.12 \times 10^{-15} \text{ erg cm}^{-2} \text{ s}^{-1}$ ). The position of the peak fibre is marked by a cross in the velocity image, and the orientation of the radio source axis is marked by a thick line. The position of the edge of the hexagonal ARGUS aperture is marked around each image. North is to the top and east to the left, and 2 arcsec corresponds to  $\sim 10 \text{ kpc}$  at the redshift of the quasar.

Fig 1: a disc is drawn at the position of each fibre where line emission was significantly detected – areas left blank within the outline of the ARGUS aperture have no line detection in those fibres. The greyscale colour within each disk gives the intensity of the line emission measured within that fibre’s spectrum. Fig 1 shows the [OIII] line emission to be clearly more extended than the approximate PSF given by the broad H $\beta$  image. The nebula extends out to a maximum of 4.1 arcsec (21 kpc) to the East (at p.a.  $105^\circ$ ), and to  $\sim 1.9$  arcsec ( $\sim 10 \text{ kpc}$ ) in all other directions, with the maximum dimension approximately perpendicular to the radio source axis. (1 arcsec corresponds to  $\sim 5.1 \text{ kpc}$  at the redshift of the quasar, assuming the cosmology of  $H_0=50 \text{ km s}^{-1} \text{ Mpc}^{-1}$  and  $q_0=0.5$  which will be used throughout this paper).

Redshifted [OII] $\lambda$ 3727 line emission is barely detected in the EELR, even when the spectra are binned into larger 7-fibre cells, as it falls in the less sensitive region of the combined chip+grism response. Narrow H $\beta$  is also too faint to be significantly detected outside of the nuclear regions in individual fibres. We obtain an off-nuclear detection of each of [OII] and H $\beta$  only by summing the spectra from 20 fibres forming the most extended region at the SE of the nebula (the fibres marked by diamonds in Fig 2). Fitting the total spectrum from this region enables us to obtain average line fluxes (although [OII] had to be fixed at the same velocity width as the [OIII] and H $\beta$  complex) and thus intensity ratios of [OIII]/H $\beta$  and [OII]/[OIII] (Table 2 and Fig 4). We calculate the fractions of total line emission emitted from the nucleus (defined as emitted by the central 19 fibres) in the both [OIII] and [OII] and find them to be 69 and 52 per cent respectively (Table 3). These may well represent underestimates of the actual fractions, as we do not take into account any EELR that may be contributing emission along the line of sight to the quasar nucleus.

Fig 1 also shows the radial velocity of the [OIII] $\lambda$ 5007

Please see separate figure

**Figure 2.** Outline of the nebula associated with 3C323.1, with diamonds marking the 20 fibres used to calculate average values of line intensity ratios given in Table 2. The asterisk marks the peak fibre, and the straight lines show the position angles of the three cuts at  $90^\circ$ ,  $120^\circ$  and  $150^\circ$  along which values of both intensity and radial velocity of the [OIII] $\lambda$ 5007 line are shown in Fig 3.

line relative to that the peak fibre. The nebula appears to show a fairly regular dipolar motion with amplitude of  $\pm 200 \text{ km s}^{-1}$ , albeit about an axis misaligned from that of the radio source by approximately 25 degrees. The radial velocity values along cuts at position angles of  $90^\circ$ ,  $120^\circ$  and  $150^\circ$  (as marked in Fig 2) are shown in Fig 3. The linewidth (FWHM as measured from the fit to the [OIII] lines) is highest around the nucleus, dropping to  $200\text{--}400 \text{ km s}^{-1}$  in the extended emission to the SE.

### 3.2 4C11.72, $z=0.323$

4C11.72 is a relatively compact (diameter  $\sim 75 \text{ kpc}$ ), linear radio source associated with a low-redshift quasar located in a small cluster of galaxies (Gunn 1971; Robinson & Wampler 1972; Yee & Green 1984; Block & Stockton 1991; Ellingson et al. 1994). The quasar lies in a relatively undisturbed host galaxy (Hutchings & Neff 1992), but has an [OIII] emission-line region extended along position angle  $100^\circ$ , with an orientation and a spatial scale comparable to the radio source (SM87; Hutchings & Crampton 1990; Durret et al. 1994). 4C11.72 is the best case amongst low-redshift quasars for an association between the EELR and radio emission, although not all the ionized gas is related to the radio structure. The EELR is clumpily distributed, with two bright concentrations  $\sim 4$  arcsec south-east of the quasar nucleus, spatially coincident with a radio lobe. Spectroscopy of the EELR shows the gas to have an irregular and chaotic velocity structure throughout the envelope, with a range in velocities of a few hundred  $\text{km s}^{-1}$  (Hutchings & Crampton 1990; Durret et al. 1994).

The EELR extends right to (and probably beyond) the edges of the ARGUS aperture to the south and north-west (Fig 5). The [OIII] $\lambda$ 5007 line emission from the quasar is spatially extended along an approximate south-east to north-west direction forming a rhomboidal shape of approximate size  $8 \times 6$  arcsec ( $\sim 45 \times 35 \text{ kpc}$ ; 1 arcsec corresponds to  $5.7 \text{ kpc}$  at the redshift of the quasar). The image of the nucleus of this quasar in both the light of [OIII] $\lambda$ 5007 and broad H $\beta$  is asymmetric (this is a real variation in the intensity of the emission lines between each fibre and not an artefact caused by the differential response of fibres themselves). The quasar is again at too low a redshift for the [OII] $\lambda$ 3727 to be detectable, as it lies in the least sensi-

**Table 2.** Average line ratios in the EELR of the quasars *except* for 4C37.43 whose line ratios are shown in Fig 13.

Quasar	Distance from nucleus (kpc)	[OII]/[OIII]	[OIII]/H $\beta$
3C323.1	14 $\pm$ 4 (SE)	0.7 $\pm$ 0.3	4.1 $\pm$ 0.7
4C11.72	20 $\pm$ 6 (E)	0.6 $\pm$ 0.2	6.6 $\pm$ 1.9
	24 $\pm$ 7 (SE)	<0.4	20.8 $\pm$ 14.8
	22 $\pm$ 5 (S)	0.4 $\pm$ 0.2	14.5 $\pm$ 9.2
3C215	13 $\pm$ 5 (N)	< 0.8	> 4.7
3C334	22 $\pm$ 1 (outer)	0.3 $\pm$ 0.1	10.8 $\pm$ 4.1
	14 $\pm$ 6 (inner)	0.3 $\pm$ 0.1	>4.5
3C281	15 $\pm$ 4 (NW)	0.3 $\pm$ 0.1	>5.9

Notes: The errors on the intensity ratios given are not the extrema, but are propagated from the  $\Delta\chi^2=1$  errors on the intensity in the line fits.

tive part of the chip+grism response. We have instead divided the south-east EELR into three (approximately) equal wedges to the east, south-east and south (Fig 6), well beyond the nuclear light spillover, and have summed the fibre spectra to give an average spectrum in each of the three regions. The [OII] $\lambda$ 3727 line was clearly detectable in the two of these regions, and we obtain an upper limit to it in the SE region, fixing its width and redshift to be the same as that fitted to the [OIII] $\lambda$ 5007 line complex. The average line intensity ratios derived are shown in Table 2 and Figure 4.

At first sight, the radial velocity of the EELR appears to have an approximately dipolar structure about an axis almost perpendicular to the radio source axis. The [OIII] line is redshifted by about 200 km s $^{-1}$  to the north-west of the nucleus, but the south-eastern side is uneven, with a region of blueshifted material with velocities ranging over  $-200$  km s $^{-1}$  to  $-400$  km s $^{-1}$  to the south (Fig 5). The velocity structure we observe is in agreement with that found by Hutchings & Crampton (1990) and Durret et al. (1994). There is a particularly close correspondence between the radio source structure where it is co-spatial with the EELR to the south of the quasar nucleus; the most strongly blueshifted gas is directly spatially coincident with the double radio hotspot 2.4 arcsec south-east of the quasar nucleus (Fig 7). This correspondence naively suggests a direct physical interaction between the radio and optical plasmas in this region, but the linewidth of [OIII] remains relatively narrow ( $< 500$  km s $^{-1}$ ) in this region, increasing to  $\sim 900$  km s $^{-1}$  only around the nucleus (Fig 5). The ionization state of the gas is, however, slightly higher in this region to the south than that more to the east of the quasar nucleus (Fig 4 and Tab 2).

### 3.3 4C37.43, $z=0.371$

4C37.43 has one of the most spectacular and luminous EELRs known around a low-redshift quasar, with a full extent of 200 kpc (SM87). The EELR is distributed into two main condensates away from the quasar itself; a large cloud centred 3.4 arcsec (21 kpc at a redshift of 0.371) directly east of the quasar nucleus, and a thin elongated cloud running north-east to south-west centred 3.4 arcsec to the north-west of the quasar (Fig 9; SM87). Durret et al. (1994) show that these two main regions have velocity fields which can each be ascribed to a simple rotating disk decoupled from the rest

of the line emission. The continuum structure around the quasar is also complex, with a faint companion galaxy lying 10 arcsec east, perhaps linked to the quasar by a straight continuum ‘bridge’, and an elongated galaxy just beyond the emission cloud at  $\sim 6$  arcsec to the north-west (Block & Stockton 1991). The distribution of the continuum- and line-emitting material appears completely uncorrelated; in particular both clouds have no associated continuum. The quasar may be associated with a small group of galaxies (Yee & Green 1984; Ellingson et al. 1994). The radio source associated with the quasar is a straight and symmetric FR II double source, with the hotspots separated by  $\sim 60$  arcsec (370 kpc) at a position angle of  $110^\circ$  (Miller, Rawlings & Saunders 1993).

We centred our ARGUS aperture directly on the quasar, covering both the eastern and north-western gas clouds, but not the extended continuum structure around this quasar. Fig 9 shows our reconstructed ARGUS image of the quasar in the light of both [OIII] $\lambda$ 5007 and broad H $\beta$  (to show the nuclear/instrumental PSF). The off-nuclear condensates are apparent in [OIII] (see also Figs 10 and 11) and both they and the quasar seem to be embedded in a low-level diffuse emission.

The radial velocity map of the [OIII] line emission (Fig 9) is again very consistent with that published from field spectroscopy by Durret et al. (1994). The eastern cloud is blueshifted by  $\sim 200$  km s $^{-1}$  relative to the nucleus, and the north-western cloud by  $\sim 400$  km s $^{-1}$  (Figs 10, 12), although both show a slight gradient across the cloud, increasing to  $-300$  and  $-500$  km s $^{-1}$  respectively towards the south.

It is interesting to compare the location and velocity gradient of the EELR to the radio source structure, as both major condensations cross the radio axis. In particular, the most blueshifted regions in each cloud spatially coincide with the radio source axis. The nature of any relation between the radio source and the optical line emission is far from obvious, as the radio lobes lie far beyond the visible emission-line region. In addition, the FWHM of the [OIII] line is lower in the eastern cloud than at the nucleus ( $< 300$  km s $^{-1}$  as opposed to  $500$ - $600$  km s $^{-1}$  on-nucleus; Fig 12), suggesting little turbulence of the gas here. The off-nuclear gas is at much higher FWHM in the southern end of the elongated north-western gas cloud, however, reaching widths of  $700$ - $800$  km s $^{-1}$  where it crosses the radio source axis (Figs 9,

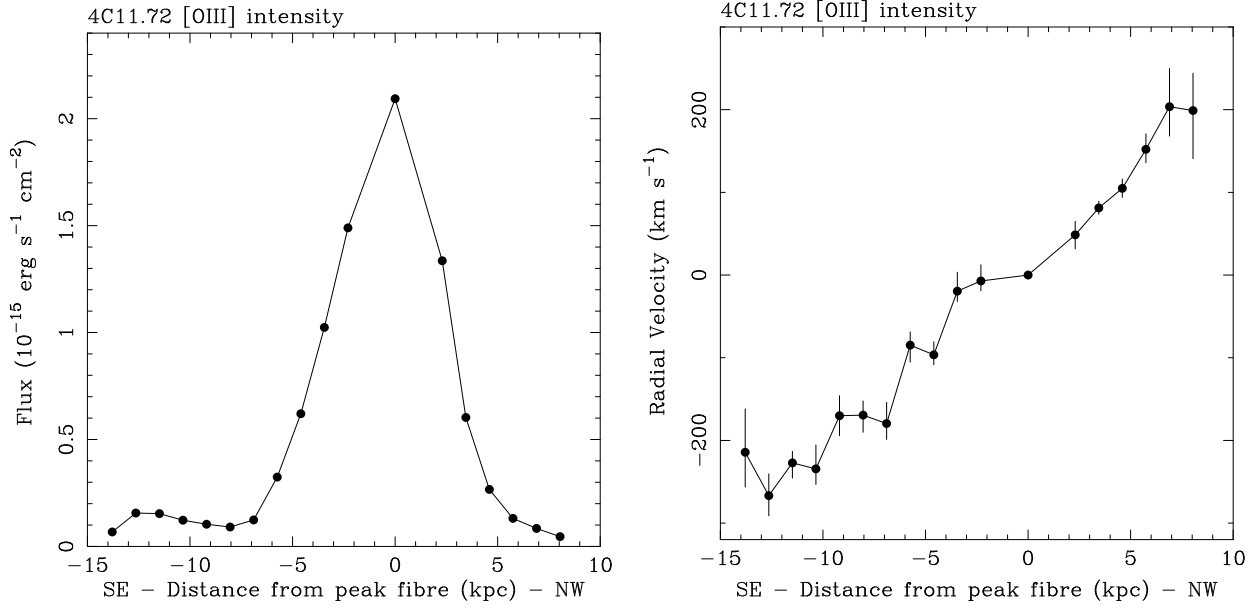


**Figure 8.** The intensity (left) and the radial velocity relative to the peak fibre (right) of the  $[\text{OIII}]\lambda 5007$  line emission along a cut following a position angle of  $150^\circ$  through the nebula of 4C11.72. The errors on the radial velocity map are the  $\Delta\chi^2=1$  confidence values from the fits to the emission lines and do not take systematics that may be introduced by the data reduction into account.

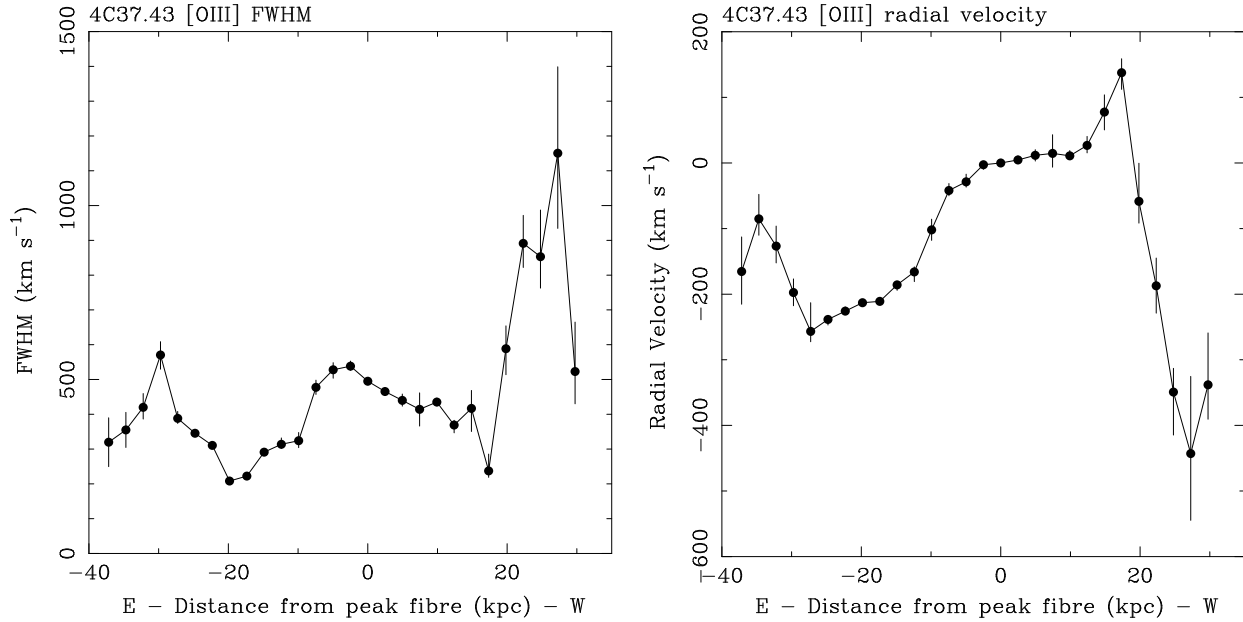


**Figure 12.** The FWHM (left) and the radial velocity relative to the peak fibre (right) of the  $[\text{OIII}]$  line emission along an E-W cut through the nebula of 4C37.43. The errors on the radial velocity map are the  $\Delta\chi^2=1$  confidence values from the fits to the emission lines and do not take systematics that may be introduced by the data reduction into account.

12). This is also the region in the EELR showing the largest blueshift ( $-500 \text{ km s}^{-1}$ ).

Narrow  $\text{H}\beta$  is detectable in individual fibres covering the core of the eastern emission-line cloud, and the  $[\text{OIII}]/\text{H}\beta$  intensity ratio here is markedly higher than around the nucleus (Fig 9). Due to the combination of low quantum efficiency of the Loral 3 detector and the O300 grism at blue wavelengths, the  $[\text{OII}]\lambda 3727$  emission line is too faint to detect in individual fibre spectra covering the extended line emission. Instead we have summed the fibres into larger cells

each of seven fibres to gain a better detection of  $[\text{OII}]$  off-nucleus. Where all of  $[\text{OII}]\lambda 3727$ ,  $[\text{OIII}]\lambda 5007$  and narrow  $\text{H}\beta$  emission lines are detected within our aperture, we have formed the line ratios and plot them in a standard diagnostic diagram (Fig 13). The observed line ratios in the eastern cloud agree well with the average values obtained by D94 and CF89.

### 3.4 3C215, $z=0.412$

3C215 lies in a densely clustered environment (Hintzen 1984; Ellingson, Yee & Green 1991) and the radio source has a very complex structure. A knotted jet emerges from the nucleus to the east (pa  $77^\circ$ ), but the other main radio features on this side lie along an angle of  $100^\circ$  from the nucleus, as if the jet had been deflected by about  $40^\circ$  toward the south-east after 3.6 arcsec (Bridle et al. 1994). The lobe of this and the other side of the radio source are both very distorted. CF89 showed from long-slit spectroscopy that the oxygen line emission from the quasar was extended toward the north. Narrow-band imaging in the light of redshifted [OII] $\lambda 3727$  shows an extension in the nebula for about  $\sim 2$  arcsec along a position angle of  $30^\circ$  (Hes et al. 1996). Narrow-band [OIII] imaging by Hutchings (1992) did not show the host nebulosity, but indicated the presence of three emission-line clouds at further radii, associated with the radio source structure in some way.

The spectrum of the broad components to the Balmer lines within the nucleus of this quasar are particularly difficult to fit in QDP, as there appears to be a large blueshifted component to the broad lines (Brotherton 1996). We have fitted the [OIII] and narrow  $H\beta$  complex, without using a complicated fit to the broad  $H\beta$  line. Thus instead of quantifying the nuclear PSF for this observation by means of the broad  $H\beta$  line intensity, we have used a region of nearby featureless continuum between 7200–7500Å (observed; corresponding to 5100–5312Å at rest wavelengths). In the light of [OIII] $\lambda 5007$ , this quasar shows only a marginal extension out to a radius of 2.5 arcsec (17 kpc) directly towards north (Fig 14; note that the image of this quasar is rotated by  $45^\circ$  compared to the rest of the quasars in this paper), but it is not extended in the light of either [OII] $\lambda 3727$  or narrow  $H\beta$ . There is no substantial velocity shift (ie  $< 150 \text{ km s}^{-1}$  with respect to the nuclear velocity) anywhere within the [OIII] nebula. We obtain only limits to the [OII] and narrow  $H\beta$  line emission from the sum of eleven fibre spectra comprising this northern extension, and thus only limits to the intensity ratios (Table 2). These ratios are, however, consistent with the previous findings of CF89 who measured [OII]/[OIII] of  $0.5_{-0.2}^{+0.4}$  at  $29 \pm 6$  kpc and  $1.3_{-0.6}^{+4.0}$  at 40 kpc from a long slit spectrum oriented in the same direction from the nucleus. There is no obvious structure in the FWHM of the [OIII] $\lambda 5007$  line across the system.

### 3.5 3C334, $z=0.555$

3C334 lies in a clustered environment (Hintzen 1984; Yee & Green 1987), and is associated with a large double radio source with a very strong jet to the south-east of the nucleus. CF89 showed from long-slit spectroscopy that the oxygen emission lines are extended north-south of the quasar. Hes et al. (1996) claim that the light of redshifted [OII] is closely aligned with the direction of the strong radio jet (see also Hes 1995). Imaging in [OIII] by Lawrence (1990), however, shows the strongest line emission extended out to the north of the quasar by several arcseconds.

Fitting the [OIII]+ $H\beta$  complex in 3C334 requires special care, as two atmospheric absorption bands around 7600Å cut into the red wing of the broad  $H\beta$  emission component, between the narrow  $H\beta$  and [OIII] $\lambda 4959$  emission

lines. The absorption bands were included in the fit as two gaussians when visible against the broad  $H\beta$  and continuum. The narrow emission-line gas (principally [OIII]) is clearly extended into a plume stretching 4 arcsec ( $\sim 30$  kpc) to the north of the quasar (Fig 15), with little sign of the extension to the south-east (and out of the aperture). It is less extended in [OII] $\lambda 3727$  and narrow  $H\beta$ . The northern plume is slightly redshifted (by about  $100 \text{ km s}^{-1}$ ) and at a lower linewidth (around  $350 \text{ km s}^{-1}$ ) than the gas closer to the quasar nucleus, with the whole nebula forming essentially a static system. The nuclear line emission has high linewidths ( $800\text{-}1000 \text{ km s}^{-1}$ ), and is very slightly blueshifted to the east of the nucleus.

The images in [OII] and [OIII] peak in neighbouring fibres due to slight atmospheric refraction during the observation. Thus we have been careful in forming line intensity ratios in the northern extended emission, forming average ratios from two large cells within the nebula where the extended emission in both lines is clearly significant. We average seven fibres centred at a projected distance of 14 kpc north of the nucleus (the ‘inner’ region) and another 3 fibres 22 kpc north (the ‘outer’ region: Table 2).

### 3.6 3C281, $z=0.599$

3C281 is associated with a large (330 kpc lobe separation) linear steep spectrum radio source (Bogers et al. 1994), whose host quasar is known to lie in a rich cluster (Yee & Green 1987). Long-slit spectroscopy by Bremer et al. (1992) showed it to have extended [OII] and [OIII] emission out to 5–8 arcsec to the south of the quasar.

Our image shows the [OII] and [OIII] line-emitting gas only marginally extended, out to 2.5 arcsec NW (corresponding to a projected distance of 19 kpc) from the quasar nucleus (Fig 16). Curiously we do not find any emission to the south of the quasar, in contradiction to the spectroscopic findings of Bremer et al. (1992). The orientation of the slit in Bremer et al. is not in doubt (given another two objects also aligned within the slit), but further direct comparison to our results is hampered by the lack of a detection limit in that paper. The gas in the North-west extended region is redshifted by about  $300 \text{ km s}^{-1}$  relative to the nucleus, and there is no discernible structure to the linewidth across the EELR. We sum seven fibres in this off-nuclear region to measure average line intensity ratios for the EELR (Table 2).

## 4 SUMMARY AND DISCUSSION

### 4.1 Morphology

The quasar nebulosities presented show both smooth (eg 3C323.1) and clumpy (eg 4C11.72, 4C37.43) distributions, and none are particularly symmetric about the radio axis. 3C334 and 3C215 both show plumes of emission, and 3C281 shows only an indistinct elongation to one side. Nearly all of the quasars are associated with large ( $> 200$  kpc) radio sources, and in all but the exception (4C117.2, with a radio source diameter  $< 100$  kpc) the extent of the optical emission is very much smaller (typically around ten per cent; though note that both 4C37.43 and 4C11.72 are known to extend out of the ARGUS aperture at lower flux levels;

**Table 3.** Properties of the line emission from the quasars and the radio source.

Quasar	L([OII]) ( $10^{43}$ erg s $^{-1}$ )	L([OIII]) ( $10^{43}$ erg s $^{-1}$ )	$\frac{L_n}{L_{tot}}$ ([OIII]) (%)	$\frac{L_n}{L_{tot}}$ ([OII]) (%)	p.a. [OIII] ( $^{\circ}$ )	max diameter [OIII] (kpc)	p.a. radio ( $^{\circ}$ )	max diameter radio (kpc)	Ref
3C215	0.05	0.54	85	90	10	25	77*, <sup>†</sup> (328)	205	Br
3C281	0.25	1.86	64	73	290	29	11	330	Bo
4C37.43	0.11	3.10	33	61	105	62 <sup>‡</sup>	110	375	Mi
3C323.1	0.13	1.63	69	52	115	32	20	360	Bo
3C334	0.62	5.13	68	63	355	41	140 <sup>†</sup> (310)	460	Br
4C11.72	0.55	1.89	37	29	110	54 <sup>‡</sup>	138	75	Mi

**Notes to Table:**

The luminosities of the total [OII] $\lambda$ 3727 and [OIII] $\lambda$ 5007 line emission are given in columns 2 and 3 for each quasar.

The ratio of nuclear to total luminosity in both [OII] $\lambda$ 3727 and [OIII] $\lambda$ 5007 are given in columns 4 and 5, where the ‘nuclear’ luminosity is measured from the total spectrum extracted from the 19 fibres around the peak fibre.

The position angle of the the optical nebula (column 6) is estimated to within  $\pm 10^{\circ}$ .

\* Radio jet is deflected to a position angle of  $100^{\circ}$  after 3.6 arcsec.

<sup>†</sup> Position angle of inner jet only; position angle of counter jet-side follows in brackets.

<sup>‡</sup> Optical nebula extends out of the ARGUS aperture.

References for radio maps are given in the final column: (Bo) 1.4GHz Bogers et al. 1994; (Br) 4.9GHz Bridle et al. 1994; (Mi) 4.9GHz Miller et al. 1993

SM87). Although estimating a position angle for the main orientation of the nebulae is subjective (and only good to within  $\pm 10^{\circ}$ ; Table 3), we find a range of behaviour with respect to the radio source orientation. Both the EELRs of 3C323.1 and 3C281 have their maximum elongation approximately perpendicular to the radio source axis, that of 4C11.72 is directly coincident with the radio source structure. The line emission around 4C37.43 shows an indistinct relation to the radio axis, while the EELR of 3C215 appears to be completely unrelated (albeit extended perpendicular to the *generic* radio source axis). We do not see any tendency for the EELR to be aligned with the radio jet in the two jetted radio sources. In general the distribution of the gas is much less anisotropic than that around radio-loud quasars at higher redshift where the alignment effect is observed (Heckman et al. 1991a; Ridgway & Stockton 1998).

For several of the systems presented, a large fraction of the total line luminosity is emitted from the EELR. In two cases (4C11.72 and 4C37.43) about two-thirds of the total [OIII] $\lambda$ 5007 is emitted from the EELR; a similar proportional distribution is seen for the [OII] $\lambda$ 3727 in 4C11.72, where as one-third of the total [OII] is off-nuclear in 4C37.43. Apart from 3C323.1 where about a half of the total [OII] and a third of the total [OIII] are emitted by the EELR, a similar proportional distribution is seen between the [OII] and [OIII] in the rest of the quasars (3C334  $\sim$  65 per cent; 3C215  $\sim$  87 per cent and 3C281  $\sim$  68 per cent). It is thus possible that the nebula also emits along the line of sight to the nucleus, yielding a slight overestimate to the nuclear contribution to the total line luminosity.

**4.2 Kinematic behaviour**

The EELR studied show a range of kinematic behaviour, three of which are in some way related to the radio source axes. 3C323.1 displays possible bipolar rotation  $\pm 200$  km s $^{-1}$  about an axis not quite aligned with the radio source axis. Although the EELR in 4C11.72 also appears at first glance to be in general dipolar rotation  $\pm 200$  km s $^{-1}$

(albeit about an axis now perpendicular to that of the radio source), there is a region of an added strong blueshift and possibly of higher ionization where coincident with the southern radio lobe. There is no obvious increase in velocity width in this region, however, that would be indicative of an interaction between the optical and radio plasmas.

4C37.43 shows a strong blueshift with respect to the nucleus in the two major condensates either side of the quasar, which each display a possible dipolar structure about an axis directed radially out of the nucleus. This velocity structure precludes the gas we see being in simple dipolar rotation around the quasar. Although the clouds are not wholly coincident with the radio axis, it is notable that the region of largest blueshift and of higher ionization in both the East and West clouds, and the highest FWHM in the West cloud (but not the Eastern cloud) are all where the optical gas crosses the radio source axis. Whilst these may be taken as indicators in favour of a jet-cloud interaction (particularly to the north-west of the QSO), there is no obvious distortion in the radio source to support this interpretation (Miller et al. 1993). The off-nuclear clouds may simply be seen in projection against the quasar; their velocity is the expected order of magnitude to be contained in a poor cluster of galaxies. Although the blueshift could alternatively be due to an outflow (eg from the expansion of ionized gas heated in a cone around the quasar continuum beam) one would have to appeal to a very distinct geometry or obscuration to explain the lack of redshifted component.

The other three quasars appear to have kinematic behaviour that does not seem to be particularly related to the contained radio source. Even though [OIII] $\lambda$ 5007 emission around 3C281 is not very extended, it is slightly redshifted (by 300 km s $^{-1}$ ) with respect to the nucleus. 3C215 and 3C334 both appear to show essentially static systems (all within 150 km s $^{-1}$  of the nucleus).

Most of the EELR around these quasars show a consistent pattern of highest line-widths coincident with the quasar nucleus, falling to typically  $\sim 200$  km s $^{-1}$  at larger radii.

### 4.3 Ionization state

The ionization state of the emitting regions around each quasar (as defined by the line ratios between [OII] $\lambda$ 3727, [OIII] $\lambda$ 5007 and H $\beta$ ) show them to be very similar to each other (Figs 4 and 13), implying that the ionization of the EELR occurs within a relatively homogeneous set of physical conditions. The line ratios and lack of correlation with any extended continuum structure (SM87) argue against the gas being ionized *in situ* by hot stars. Given the proximity to a luminous quasar nucleus, one can assume that illumination by the UV continuum of the active nucleus provides the *minimum* source of ionization. The fact that the morphology of the gas is not in all cases strongly aligned with the radio source axis implies that the quasar UV radiation is not strongly confined (either by beaming or shielding) to escape only along this axis.

The only regions of higher ionization observed are those directly coincident with the radio source axis, most notable to the eastern side of 4C37.43 and more marginally to the south-east of 4C11.72. Unlike the case of 3C254 (Crawford & Vanderriest 1997) there is no *clear* evidence for a jet-cloud interaction to be occurring in these regions (*i.e.* the *combination* of increased line-width, distorted radio structure, a large velocity gradient). We note, however, that any shocks caused by compression where the EELR is spatially coincident with the radio plasma in these regions will only add to the default photo-ionization provided by the quasar.

### 4.4 Pressure Estimates

Assuming that the dominant source of ionization for the emitting gas is the UV continuum of the quasar nucleus, we can use the line intensity ratios observed in the EELRs to infer physical properties of the emitting gas. We match the observed ratios to those obtained from photoionization modelling using CLOUDY 90.04 (Ferland 1996), assuming the nuclear continuum is not very different from that we see, and that the gas lies at the projected separation from the nucleus (see *eg.* Forbes et al. 1990; Crawford et al. 1991 for a more detailed discussion of this technique and the assumptions thereof).

We estimate the shape of the ionizing continuum from archival ultraviolet HST and X-ray ROSAT PSPC spectral data of the quasars. We first fit the 1050-3000Å HST spectrum (corrected for Galactic reddening) by a power-law of slope  $\alpha_{UV}$ , where  $f_\nu \propto \nu^{\alpha_{UV}}$ . [If defining the continuum level is complicated by the presence of broad emission bands and lines, we fit the spectrum using only the continuum bands listed by Zheng et al. (1997)]. Similarly we fit the 0.2–2 keV ROSAT PSPC spectrum by a power-law slope of  $\alpha_X$ ; none of the quasars in this sample required any significant absorption above that expected from the line-of-sight Galactic column density. There is a problem, however, in that the ROSAT PSPC consistently measures power-law slopes that are *steeper* by  $\Delta\alpha_X \sim 0.5$  than is derived from observations of the same objects by other X-ray missions (Fiore et al. 1994; Laor et al. 1997; Iwasawa, Fabian & Nandra 1999). We correct for this effect by assuming X-ray slopes shallower by  $\Delta\alpha_X \sim 0.5$  than we fit from the PSPC spectra. For the two quasars with no PSPC observation (4C11.72 and 3C281) we assume the X-ray continuum to follow the canonical power-

law slope for a radio-loud quasar of  $\alpha_X = -0.5$  (Schartel et al. 1996; Laor et al. 1997 and taking into account the artificially steep slopes that ROSAT measures), and fix the relative normalization between the UV and X-ray bands from the ROSAT X-ray flux given by Brinkmann et al. (1995).

We thus represent the nuclear continuum over the UV/X bandwidths by power-laws of slopes  $\alpha_{UV}$  and  $\alpha_X$ , with the relative normalization fixed so that  $\alpha_{OX}$  (the slope between 2500Å – 2 keV; see *eg.* Zamorani et al. 1981) fits the observed fluxes. The whole spectrum is normalized to the observed luminosity of the quasar. The [OIII]/H $\beta$  ratio observed in the EELR also allows us to constrain the high-energy end to any ‘Blue Bump’ component, parameterized by the temperature  $T$  of an exponential cutoff to the lower-energy continuum of slope  $\alpha_{UV}$ . The values for these parameters defining the input AGN continuum are listed for each quasar in Table 4. The situation is complicated for 4C37.43, where the higher ionization regions in some parts of the EELR (Fig 13) would require a different ionizing continuum than do the ratios from the remainder of the diffuse emission. It is probable that the higher ionization is caused by some extra source of ionization *in situ* in these regions, so we do not attempt to model these regions in detail.

The quasar continuum is assumed incident on a neutral gas cloud at the projected radius of the EELR from which the [OII]/[OIII] ratios shown in Table 2 and Figs 4 and 13 are extracted. The cloud parameters are varied in CLOUDY until the runs predict a good match to the observed line ratios. The pressures deduced within the EELR of all six quasars show a very similar and high range of values, all over  $10^5 \text{ cm}^{-3} \text{ K}$  for projected radii of 15-25 kpc from the nucleus (Figs 17 and 18). Uncertainties in these estimates are due to the errors in the [OII]/[OIII] ratio from the emission-line fitting, typically around  $\pm 35$  per cent; uncertainties in the temperature of the ‘Blue Bump’, where the errors in [OIII]/H $\beta$  could change the bump temperature and thus the inferred pressure by typically  $\pm 20$  per cent. The main potential source for error is the range in radius over which the line ratios are averaged; at the inner (outer) part of this range the same line ratio would match a gas pressure typically a factor of two greater (smaller) than that inferred. This error margin is shown by the error diamonds in the Fig 17, where the error bars represent the errors due to the uncertainty only in the measurement of the [OIII]/[OII] line ratio. Note though, that the lower limit to the temperature of the bump in 3C281 and 3C215 implies that the pressures inferred could also be greater at a given distance.

### 4.5 Interpretation of the immediate environment

The pressures inferred within the extended emission-line regions around the six quasars are all compatible with those measured in the intracluster medium of nearby clusters of galaxies. Furthermore, the range of pressures deduced are consistent with a moderate cooling flow (of tens to a couple of hundred solar masses a year) operating in the nearby environment of the quasar. The radial pressure profile of the ionized gas around 4C37.43 has a proportionality of  $P \propto r^{-0.8 \pm 0.2}$  (Fig 18). This is compatible with the EELR being in pressure equilibrium with hot gas following the  $\sim r^{-1}$  distribution expected for distributed mass deposition in an isothermal halo. For comparison, in Fig 18 we also plot

**Table 4.** Nuclear ionizing continuum

Name	$\alpha_{UV}$	$\alpha_X$	$\alpha_{OX}$	$T$ ( $10^5\text{K}$ )
3C323.1	-0.6	-1	-1.4	2.5
4C11.72	-0.9	-0.5	-1.6	10
4C37.43	0	-0.7	-1.4	2.25
3C215	-0.5	-0.5	-1.1	>3.5*
3C334	-0.5	-0.8	-1.45	6.5
3C281	-1	-0.5	-1.2	>3*

$\alpha$  for all bands is defined as  $f_\nu \propto \nu^\alpha$ .

$\alpha_X$  has been corrected for the over-steepening of PSPC spectra of  $\Delta\alpha_X \sim 0.5$ , as mentioned in the text.

\*  $T$  can only be constrained to be a lower limit where only a lower limit to the [OIII]/H $\beta$  ratio can be measured.

the pressure profile derived from a deprojection of ROSAT HRI X-ray data of A3581 from Johnstone, Fabian & Taylor (1998). A3581 is an interesting analogy to 4C37.43, as it is a poor cluster, hosting the FR II radio source PKS1404-267 at its core. The X-ray data show a moderate cooling flow with a mass deposition rate of  $\sim 80 M_\odot \text{yr}^{-1}$  to be occurring within the intracluster medium. The similarity of its pressure profile to our optically-deduced ones supports the inference of a cooling flow around these quasars, despite the fact that only three (3C215, 3C281 and 3C323.1) lie in environments that can be classified from field optical galaxy counts as richer than Abell class 0 (Ellingson et al. 1991; Yee & Green 1984, 1987; 3C334 and 4C11.72 lie less clustered regions, and 4C37.43 lies in a comparatively sparse environment.) In a hierarchical model for the evolution of clusters, it may well be that quasars – and their relatively undisturbed cooling flows – can only survive to lower redshifts in the *poorer* clusters that are sufficiently isolated to have so far escaped merging with richer systems (see e.g. Fabian & Crawford 1990).

Our interpretation is also supported by the recent direct detections of the X-ray emission from the host clusters of 3C215, 3C281 and 3C334 (among a handful of such detections; Crawford et al. 1999; Hardcastle & Worrall 1999) support this suggestion. In these cases, the extended X-ray component is consistent with thermal emission from the intracluster medium of moderately rich host clusters to the quasars, with inner regions dense enough to be part of a cooling flow.

#### 4.6 Relation of the EELR to the radio source

Five out of six of our quasars are associated with radio sources that are over 200 kpc in diameter (Table 3). Amongst these are three with settled or quiescent kinematic behaviour (3C323.1, 3C334 and 3C215), and one with a little (3C281) and one with a large (4C37.43) amount of velocity structure. The quasar with the smallest contained radio source, 4C11.72, not surprisingly has the most kinematically active EELR. Naively this mostly conforms to the similar division of behaviour seen in the emission-line nebulae of higher-redshift radio galaxies by Best et al. 1999, whereby the radio sources with smaller linear sizes ( $\leq 150$  kpc) show clear indications of physical interactions between the radio and optical plasmas, in terms of kinematic behaviour, ionization state and flux. Larger systems have EELRs more consistent with photo-ionization by an embedded quasar. We cannot test for the role of shock ionization in our sources as the diagnostic

UV lines are not observable at the redshifts of our sample; [OIII] $\lambda 5007$  and [OII] $\lambda 3727$  do not allow us to clearly discriminate between these possibilities. However, we note that any extra sources of ionization (such as shocks from jet-cloud interactions) will act to exacerbate the high pressures inferred from the low ionization state of the EELR. The exception to this model is the EELR around 4C37.43, which shows clear regions of higher ionization aligned along the radio axis. Although only associated with an increased FWHM to the north-west side of the quasar, it is possible that extra ionization in the form of shocks may produce this ionization differential within the nebula.

## 5 CONCLUSIONS

We have presented two-dimensional maps of the distribution, velocity structure and ionization state of the extended emission-line regions around six intermediate-redshift quasars. The EELRs show a diverse behaviour in morphology – including relation to the radio source axis – and kinematics. Despite this, they all have surprisingly similar – and low – ionization, as measured by the ratio of [OIII] $\lambda 5007$  and [OII] $\lambda 3727$ . We thus infer a confining medium around all the quasars to sustain the EELR at such low ionization in the proximity of a strong ionizing quasar nucleus.

## 6 ACKNOWLEDGMENTS

CSC thanks both the PPARC and the Royal Society for financial support while this work was in progress. This research has made use of the NASA/IPAC Extragalactic Database (NED) which is operated by the Jet Propulsion Laboratory, California Institute of Technology, under contract with the National Aeronautics and Space Administration. We have also made use of data obtained from the Leicester Database and Archive Service at the Department of Physics and Astronomy, Leicester University.

## REFERENCES

- Bahcall J. N., Kirhakos, S., Saxe D. H., Schneider D. P., 1997, ApJ, 479, 642
- Best P., Longair M. S., Rottgering H. J. A., 1998, MNRAS, 295, 549
- Best P., Rottgering H. J. A., Longair M. S., 1999, MNRAS, in press (astro-ph/9908211)

- Block D. L., Stockton A., 1991, *AJ*, 102, 1928
- Bogers W. J., Hes R., Barthel P. D., Zensus J. A., 1994, *A&AS*, 105, 91
- Bohlin R. C., Savage B. D., Drake J. F., 1978, *ApJ*, 224, 132
- Boisson C., Durret F., Bergeron J., Petitjean P., 1994, *A&A*, 285, 377
- Bower R., Smail I., 1997, *MNRAS*, 290, 292
- Bremer M. N., Crawford C. S., Fabian A. C., Johnstone R. M., 1992, *MNRAS*, 254, 614
- Bridle A. H., Hough D. H., Lonsdale C. J., Burns J. P., Laing R. A., 1994, *AJ*, 108, 766
- Brinkmann W., Siebert J., Reich W., Furst E., Reich P. Voges W., Trumper J., Wielebinski R., 1995, *A&A Suppl*, 113, 347
- Brotherton M. S., 1996, *ApJS*, 102, 1
- Canalizo G., Stockton A., 1997, *ApJLett*, 480, L5
- Cardelli J. A., Clayton G. C., Mathis J. S., 1989, *ApJ*, 345, 245
- Carilli C. L., Owen F. N., Harris D. E., 1994, *AJ*, 107, 480
- Carilli C. L. et al, 1997, *ApJS*, 109, 1
- Chatzichristou E.T., Vanderriest C., Jaffe W., 1999, *A&A*, 343, 407
- Crawford C. S., Fabian A. C., 1989, *MNRAS*, 239, 219
- Crawford C. S., Fabian A. C., 1993, *MNRAS*, 260, L15
- Crawford C. S., Fabian A. C., 1995, *MNRAS*, 273, 827
- Crawford C. S., Fabian A. C., 1996a, *MNRAS*, 281, L5
- Crawford C. S., Fabian A. C., 1996b, *MNRAS*, 282, 1483
- Crawford C. S., Fabian A. C., Johnstone R. M., 1988, 235, 183
- Crawford C. S., Lehman I., Fabian A. C., Bremer M. N., Hasinger G., 1999, *MNRAS*, in press (astro-ph/9904371)
- Crawford C. S., Fabian A. C., George I. M., Naylor T. N., 1991, *MNRAS*, 248, 139
- Crawford C. S., Vanderriest C., 1996, *MNRAS*, 283, 1003
- Crawford C. S., Vanderriest C., 1997, *MNRAS*, 285, 580
- Deltorn J. -M., Le Fevre O., Crampton D., Dickinson M., 1997, *ApJ*, 483, L21
- Dickinson M., 1997 *HST and the High Redshift Universe*, eds Tanvir N., Aragon-Salamanca A., Wall J.V., published by World Scientific.
- Dickinson et al. 1999, submitted to *ApJ*
- Durret F., Pecontal E., Petitjean P., Bergeron J., 1994, *A&A*, 291, 392
- Ellingson E., Yee H. K. C., Bechtold J., Dobrzycki A., 1994, *AJ*, 107, 1219
- Ellingson E., Yee H. K. C., Green R. F. 1991, *ApJ*, 371, 49
- Fabian A. C., 1994, *ARAA*, 32, 277
- Fabian A. C., Crawford C. S., 1990, *MNRAS*, 247, 439
- Ferland G. J., 1996, *Hazy, a Brief Introduction to Cloudy*, University of Kentucky Department of Physics and Astronomy Internal Report, University of Kentucky
- Fiore F., Elvis M., McDowell J. C., Siemiginowska A., Wilkes B. J., 1994, *ApJ*, 431, 515
- Forbes D. A., Crawford C. S., Fabian A. C., Johnstone R. M., 1990, *MNRAS*, 244, 680
- Gunn J., 1971, *ApJLett*, 164, L113
- Garrington S. T., Conway, R. G., 1991, *MNRAS*, 250, 198
- Hardcastle M., Worrall D. M., 1999, *MNRAS* in press, (astro-ph/9907034)
- Heckman T. M., Lehnert M. D., van Breugel W. J. M., Miley G. K., 1991a, *ApJ* 370, 78
- Heckman T. M., Lehnert M. D., Miley G. K., van Breugel W. J. M., 1991b, *ApJ* 381, 373
- Hes R., 1995, Ph.D. Thesis, University of Groningen
- Hes R., Barthel P. D., Fosbury R. A. E., 1996, *A&A*, 313, 423
- Hickson P., Hutchings J. B., 1987, *ApJ*, 312, 518
- Hill G. J., Lilly S. J., 1991, *ApJ*, 367, 1
- Hintzen P., 1984, *ApJSuppl*, 55, 533
- Hintzen P., Scott J. S., 1978, *ApJL*, 224, L47
- Hutchings J. B., 1992, *AJ*, 104, 1311
- Hutchings J. B., Crampton D., 1990, *AJ*, 99, 37
- Hutchings J. B., Johnson I., Pyke R., 1988, *ApJSuppl*, 66, 361
- Hutchings J. B., Neff S. G., 1992, *AJ*, 104, 1
- Iwasawa K., Fabian A. C., Nandra K., 1999, *MNRAS*, 307, 611
- Johnstone R.M., Fabian A. C., & Taylor G. B., 1998, *MNRAS*, 298, 854
- Laor A., Fiore F., Elvis M. J., Wilkes B. J., McDowell J. C., 1997, *ApJ*, 477, 93
- Lawrence C. R. 1990, *Parsec Scale Radio Jets*, eds Zensus J. A. & Pearson T. J., CUP, p280.
- McLeod, K. K., Rieke G. H., 1994, *ApJ*, 431, 137
- Miller P., Rawlings S., Saunders R., 1993, *MNRAS*, 263, 425
- Neugebauer G., Matthews K., Armus L., 1995, *ApJLett*, 455, L123
- Oemler A., Gunn J. E., Oke J. B., 1972, *ApJL*, 176, L47
- Ridgway S. E., Stockton A., 1998, *AJ*, 114, 511
- Robinson L. B., Wampler E. J., 1972, *ApJ*, 171, L83
- Schartel N. et al., 1996, *MNRAS*, 283, 1015
- Stark A. A., Gammie C. F., Wilson R. W., Bally J., Linke R. A., Heiles C., Hurwitz M., 1992, *ApJS*, 79, 77
- Stockton A., Ridgway S. E., 1991, *AJ*, 102, 488
- Stockton A., MacKenty J. W., 1987, *ApJ*, 316, 584 (SM87)
- Tennant A. F., 1991, *NASA Technical Memorandum*, 4301
- Vanderriest C., 1995, *ASP Conf. Ser.*, 71, 209
- Worrall D. M., Lawrence C. R., Pearson T. J., Readhead A. C. S., 1994, *ApJ*, 420, L17
- Yates M. G., Miller L., Peacock J. A., 1989, *MNRAS* 240, 129
- Yee H. K. C., Green R. F., 1984, *ApJ*, 280, 79
- Yee H. K. C., Green R. F., 1987, *ApJ*, 319, 28
- Zamorani G. et al., 1981, *ApJ*, 245, 357
- Zheng W., Kriss G. A., Telfer R. C., Grimes J. P., Davidsen A. F., 1997, *ApJ*, 475, 469

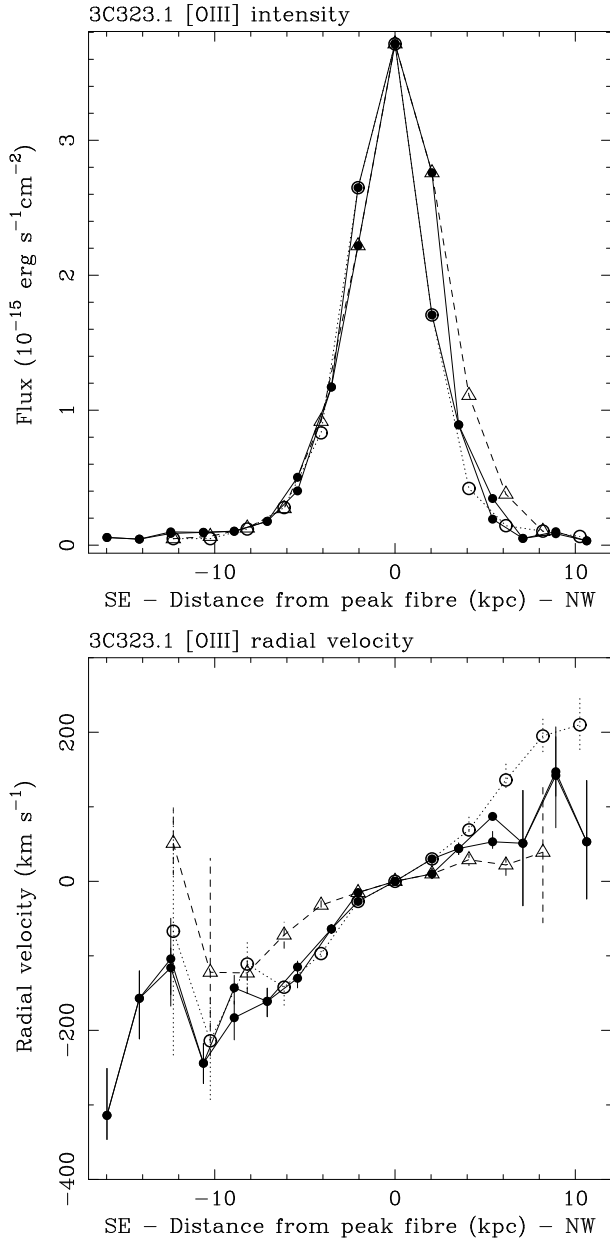


**Figure 3.** The intensity (top) and the radial velocity (below) of the [OIII] line emission relative to the peak fibre along three cuts through the nebula in 3C323.1. The dashed line marked by triangles is along the cut at  $90^\circ$ , the dotted line marked by open circles is that along  $150^\circ$ , and the solid lines and circles show the values along  $60^\circ$  (note that some of the values are double along the latter cut because it does not pass through only a single row of fibres). The width of the PSF from the nuclear line intensity varies according to whether the cut passes more along or across the rows in the hexagon. The errors on the radial velocity map are the  $\Delta\chi^2=1$  confidence values from the fits to the emission lines and do not take systematics that may be introduced by the data reduction into account.

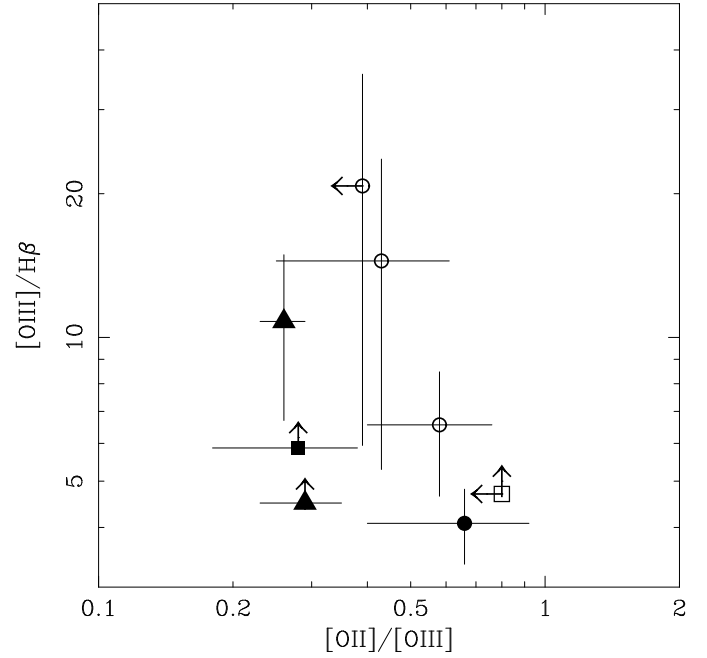


**Figure 4.** Line intensity ratios of [OIII]/ $H\beta$  plotted against those of [OII]/[OIII] for the quasar nebulosities as given in Table 2. The ratios in the extended line emission of 3C323.1 are marked by a solid circle, 4C11.72 by open circles, the limits to 3C215 by an open square, 3C334 by solid triangles and 3C281 by a solid square.

Please see separate figure

**Figure 5.** Reconstructed ARGUS images of 4C11.72 in the light of [OIII] $\lambda 5007$  line intensity (top left; on a scale of 0 (white) to a maximum (black) of  $2.09 \times 10^{-15}$  erg  $cm^{-2}$   $s^{-1}$  with minimum detection of  $0.02 \times 10^{-15}$  erg  $cm^{-2}$   $s^{-1}$ ); broad  $H\beta$  line intensity (lower left; scale  $0-7.43 \times 10^{-15}$  erg  $cm^{-2}$   $s^{-1}$  with minimum detection of  $0.10 \times 10^{-15}$  erg  $cm^{-2}$   $s^{-1}$ ); radial velocity relative to the nucleus over  $-490$  to  $360$   $km\ s^{-1}$  (top right) and FWHM (lower right;  $0-1200$   $km\ s^{-1}$ ) of the [OIII] $\lambda 5007$  emission line. The appropriate colour scale is shown to the right of each of the kinematic maps. The position of the nuclear fibre is marked by a cross in these images, and the orientation of the radio source axis is marked by a thick line in the radial velocity plot, and those fibres where the line width was unresolved are marked by a plus mark in the FWHM plot. The hexagonal ARGUS aperture is drawn around each image. North is to the top and east to the left, and 2 arcsec corresponds to  $\sim 11.5$  kpc at the redshift of the quasar.

Please see separate figure

**Figure 6.** Outline of the nebula associated with 4C11.72, with the fibres used to measure average values of line intensity ratios given in Table 2. The fibres comprising the ‘East’ region are marked by pluses, those in the ‘South-East’ region are marked by diamonds, and in the ‘South’ region are marked by crosses. The asterisk marks the peak fibre, and the straight lines mark the position angles of the cuts along  $150^\circ$  from which values of both intensity and radial velocity are shown in Fig 8.

Please see separate figure

**Figure 7.** The ARGUS image of the radial velocity structure of the extended [OIII] $\lambda$ 5007 line emission in 4C11.72. Contours of 4.86GHz radio emission from the radio source (from Miller et al. 1993) are superposed at the correct orientation and scale.

Please see separate figure

**Figure 9.** Reconstructed ARGUS intensity maps of 4C37.43 in the light of [OIII] $\lambda$ 5007 (plotted over the range  $0.02(\text{white})$ – $1.3(\text{black}) \times 10^{-15} \text{ erg cm}^{-2} \text{ s}^{-1}$ ), broad  $H\beta$  (range  $0.29(\text{white})$ – $6.77(\text{black}) \times 10^{-15} \text{ erg cm}^{-2} \text{ s}^{-1}$ ), and the ratio of [OIII]/ $H\beta$  (range 4–11). The radial velocity (from  $-550$  to  $200 \text{ km s}^{-1}$  with respect to the nucleus) and FWHM of the EELR ( $0$ – $750 \text{ km s}^{-1}$ ) as measured from the fits to the [OIII] line emission are shown to the right, each with its appropriate colour bar. The outer hexagon marks the ARGUS aperture for each image, and a cross marks the nuclear fibre in the ratio and kinematic maps. The solid line through the nucleus in the velocity map describes the direction of the radio source axis, and plus marks on the FWHM map show those fibres where the [OIII] line was unresolved. North is to the top of the image, east to the left, and 2 arcsec corresponds to a diameter of 12.4 kpc at the redshift of the quasar.

Please see separate figure

**Figure 10.** The spectrum of each individual fibre in row 12 of the 4C37.43 observation (the row crossing the nucleus; Fig 9) over the wavelength range of  $6825$ – $6925 \text{ \AA}$ , covering the spectral region of redshifted [OIII] $\lambda$ 5007; wavelength increases to the right in each panel. Fibres are numbered from east to west across the aperture, where fibre 17 marks the nuclear peak. Fibres 6–11 cover the brightest region of the large eastern cloud, fibres 14–20 show the nuclear region where broad  $H\beta$  is detected, and fibres 25–27 cover the southern end of the north-western cloud. The solid vertical line in each plot marks the observed position of the [OIII] $\lambda$ 5007 line at  $6874 \text{ \AA}$  in the nuclear fibre, to show the blueshift from that position off-nucleus. Successive fibres are centred  $0.4 \text{ arcsec}$  apart. Fibres 15–21 are plotted on a flux scale of  $0$ – $1.3 \times 10^{-16} \text{ erg cm}^{-2} \text{ s}^{-1}$ , and all other fibres on a flux scale of  $0$ – $2 \times 10^{-17} \text{ erg cm}^{-2} \text{ s}^{-1}$ .

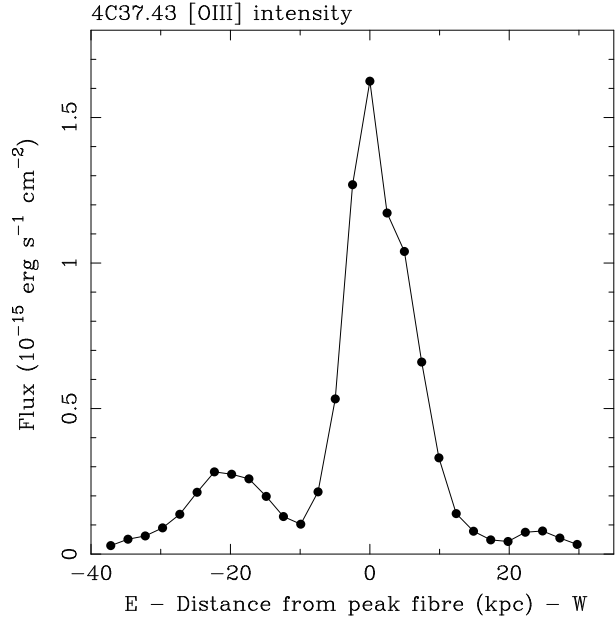


**Figure 11.** The intensity of the [OIII] $\lambda$ 5007 line emission relative to the peak fibre along an E-W cut through the nebula of 4C37.43.

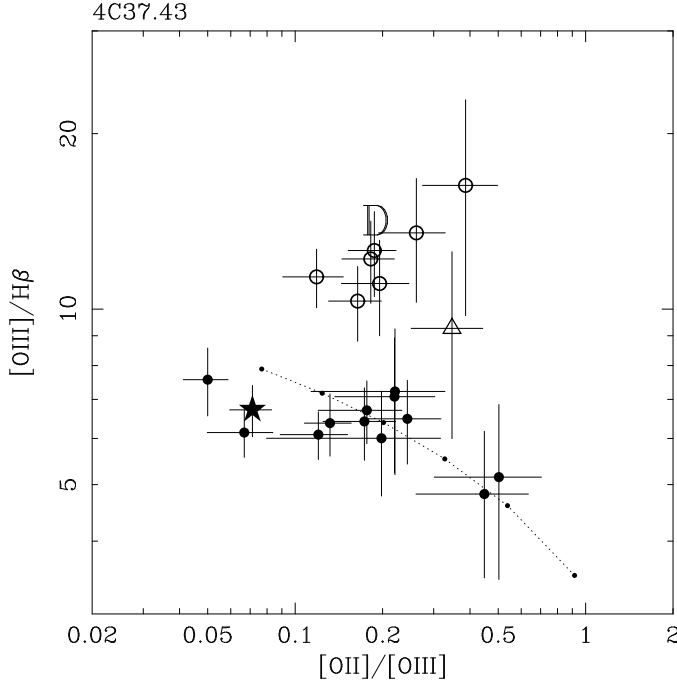


**Figure 13.** Spatially resolved line intensity ratios for the large binned cells (each of 7 fibres) for 4C37.43. The nuclear fibre is marked by a star marker, the ratios at the position of the eastern cloud are marked as open circles, and an average ratio at the north-western cloud is marked as a large triangle. The remaining points (solid circles) are those in the diffuse emission surrounding the nucleus. For comparison, the average ratios measured for the eastern cloud by Durret et al. 1994 are marked by ‘D’. The plotted line shows the range of predictions from photo-ionization calculations in CLOUDY, for a fixed density of  $100 \text{ cm}^{-3}$  and an ionization parameter decreasing from  $-1.75$  to  $-3$  from left to right, assuming a blue bump temperature of  $2.25 \times 10^5 \text{ K}$ .

Please see separate figure

**Figure 14.** Reconstructed ARGUS images of 3C215 in the light of  $[\text{OIII}]\lambda 5007$  (left; range of  $0-0.90 \times 10^{-15} \text{ erg cm}^{-2} \text{ s}^{-1}$ , where  $0.01 \times 10^{-15} \text{ erg cm}^{-2} \text{ s}^{-1}$  is the minimum detection), and in the red continuum (right; range of  $0.02-0.37 \times 10^{-15} \text{ erg cm}^{-2} \text{ s}^{-1}$ , where  $0.03 \times 10^{-15} \text{ erg cm}^{-2} \text{ s}^{-1}$  is the minimum detection). Note that in this quasar image is oriented through  $45^\circ$  with respect to the other quasars in this paper, so north-west is to the top of the plot, and north-east to the left. 2 arcsec corresponds to a distance of 13 kpc at the redshift of the quasar. The solid line in the  $[\text{OIII}]$  image indicates the direction of the jetted side of the radio source and the location of its bend with the same scale and orientation as the image (see text for details).

Please see separate figure

**Figure 15.** ARGUS images of 3C334 in the light of  $[\text{OIII}]\lambda 5007$  (range shown of  $0-2.66 \times 10^{-15} \text{ erg cm}^{-2} \text{ s}^{-1}$ , where the minimum detection is  $0.03 \times 10^{-15} \text{ erg cm}^{-2} \text{ s}^{-1}$ );  $[\text{OII}]\lambda 3727$  (range shown of  $0-0.40 \text{ erg cm}^{-2} \text{ s}^{-1}$ , where the minimum detection is  $0.02 \times 10^{-15} \text{ erg cm}^{-2} \text{ s}^{-1}$ ); narrow  $\text{H}\beta$  (range shown of  $0-0.31 \text{ erg cm}^{-2} \text{ s}^{-1}$ , where the minimum detection is  $0.01 \times 10^{-15} \text{ erg cm}^{-2} \text{ s}^{-1}$ ); broad  $\text{H}\beta$  (range shown of  $0-6.33 \text{ erg cm}^{-2} \text{ s}^{-1}$ , where the minimum detection is  $0.29 \times 10^{-15} \text{ erg cm}^{-2} \text{ s}^{-1}$ ); and in radial velocity (over the range of  $^{+150}_{100} \text{ km s}^{-1}$  relative to the nucleus). North is to the top and east to the left, and the scale bar of 2 arcsec represents a distance of  $\sim 15 \text{ kpc}$  at the redshift of the quasar. The solid line in the velocity map shows the direction of the jetted side of the radio source, and the dashed line the direction of the radio counter-jet.

Please see separate figure

**Figure 16.** ARGUS images of 3C281 in the light of  $[\text{OIII}]\lambda 5007$  (on a scale of  $0-0.69 \times 10^{-15} \text{ erg cm}^{-2} \text{ s}^{-1}$  with a minimum value of  $0.02 \times 10^{-15} \text{ erg cm}^{-2} \text{ s}^{-1}$ )  $[\text{OII}]\lambda 3727$  (on a scale of  $0-0.15 \times 10^{-15} \text{ erg cm}^{-2} \text{ s}^{-1}$  with a minimum value of  $0.02 \times 10^{-15} \text{ erg cm}^{-2} \text{ s}^{-1}$ ) and broad  $\text{H}\beta$  ( $0-2.24 \times 10^{-15} \text{ erg cm}^{-2} \text{ s}^{-1}$  with a minimum value of  $0.09 \times 10^{-15} \text{ erg cm}^{-2} \text{ s}^{-1}$ ). North is to the top and east to the left in these images, and the solid line in the  $[\text{OIII}]$  image describes the direction of the radio source axis. 2 arcsec corresponds to a distance of 15 kpc at the redshift of the quasar.

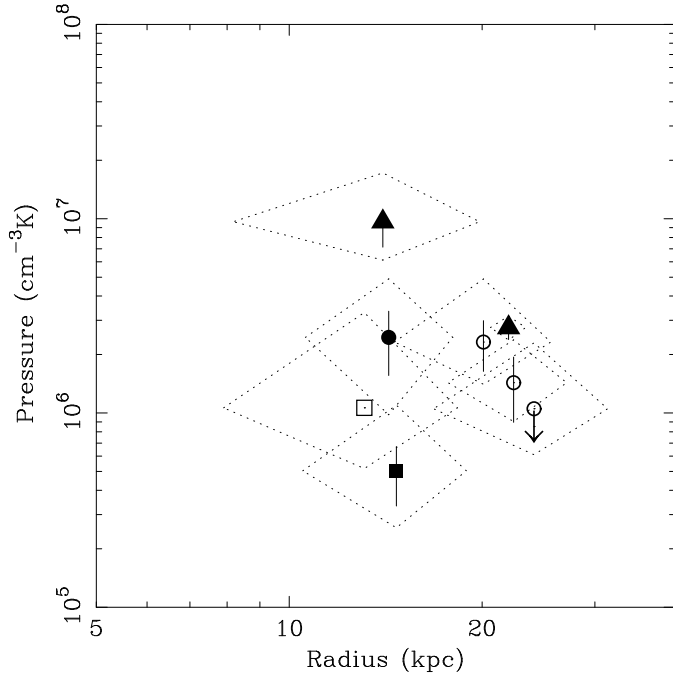


**Figure 17.** Pressures deduced from the CLOUDY runs as a function of radius from the quasar for all objects except 4C37.43 (for which see Fig 18). 3C323.1 is marked by a solid circle, 4C11.72 by open circles, the limits to 3C215 by an open square, 3C334 by solid triangles and 3C281 by a solid square. The vertical error bars only encompass the errors on  $[\text{OIII}]/[\text{OII}]$  caused by the  $\Delta\chi^2=1$  confidence values from the fits to the emission-line intensities. The larger error diamonds around each point mark the range of radius from which the line ratios have been extracted, and also the larger variation in pressure deduced if the full variation in radius is taken into account. Note that the point marked for 3C281 represents a lower limit to the derived pressure, due to our measuring only a lower limit to the  $[\text{OIII}]/\text{H}\beta$  ratio in the extended gas. This also applies for the point for 3C215; however, as we also obtain only an upper limit to  $[\text{OIII}]/[\text{OII}]$  the pressure inferred could also be less.

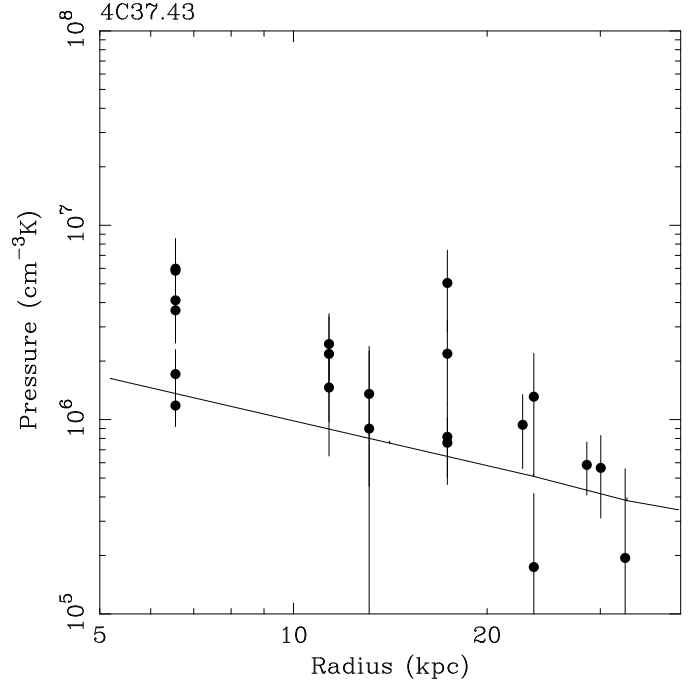


**Figure 18.** Radial pressure profile deduced from the emission line nebula around 4C37.43, excluding the higher-ionization blobs. The pressures are deduced by photo-ionization calculations in CLOUDY as described in the text, modelling the blue bump with a temperature of  $2.25 \times 10^5$  K. For comparison, the solid line shows the pressure profile within the intracluster medium around the radio source PKS1404-267 derived from X-ray observations taken with ROSAT (from Johnstone et al. 1998).

This figure "fig1.gif" is available in "gif" format from:

<http://arxiv.org/ps/astro-ph/9912306v1>

This figure "fig2.gif" is available in "gif" format from:

<http://arxiv.org/ps/astro-ph/9912306v1>

This figure "fig5.gif" is available in "gif" format from:

<http://arxiv.org/ps/astro-ph/9912306v1>

This figure "fig6.gif" is available in "gif" format from:

<http://arxiv.org/ps/astro-ph/9912306v1>

This figure "fig7.gif" is available in "gif" format from:

<http://arxiv.org/ps/astro-ph/9912306v1>

This figure "fig9.gif" is available in "gif" format from:

<http://arxiv.org/ps/astro-ph/9912306v1>

This figure "fig10.gif" is available in "gif" format from:

<http://arxiv.org/ps/astro-ph/9912306v1>

This figure "fig14.gif" is available in "gif" format from:

<http://arxiv.org/ps/astro-ph/9912306v1>

This figure "fig15.gif" is available in "gif" format from:

<http://arxiv.org/ps/astro-ph/9912306v1>

This figure "fig16.gif" is available in "gif" format from:

<http://arxiv.org/ps/astro-ph/9912306v1>